Assessment of gas hydrate and free gas distribution on the South Shetland margin (Antarctica) based on multichannel seismic reflection data

Emanuele Lodolo, Angelo Camerlenghi, Gianni Madrussani, Umberta Tinivella and Giuliana Rossi

Istituto Nazionale di Oceanografia e di Geofisica Sperimentale, Borgo Grotta Gigante 42/C, Sgonico, Trieste, 34010, Italy.
E-mail: elodolo@ogs.trieste.it

SUMMARY

Processing and interpretation of a grid of intermediate-resolution multichannel seismic reflection profiles collected on the NE sector of the South Shetland continental margin, allowed us to map the lateral extent of a Bottom Simulating Reflector (BSR). The margin, an accretionary wedge located off the northern tip of the Antarctic Peninsula, consists of two distinct and superimposed tectonic regimes: an older regime is related to Mesozoic–Middle Cenozoic subduction-related tectonism; a younger one is associated with a mainly extensional tectonic phase, and related to the Oligocene development of the western Scotia Sea. The occurrence of the BSR appears to be controlled by the geological structure of the margin. The BSR lacks continuity near basement structures, main geological discontinuities and faults. On the other hand, the amplitude and continuity of the BSR are not affected by the presence of folded structures and undeformed sedimentary layering. We found that the BSR is mostly confined to the NE sector of the South Shetland Margin, where propagation of faulting associated with the Shackleton Fracture Zone may have driven migration of natural gas towards the surface and created the conditions for a BSR to appear. The application of reflection tomography techniques allowed us to reconstruct the averaged seismic velocity field between the seafloor and BSR in order to map the depth of BSR. By averaging the observed velocity structure above and below the BSR, and applying a theoretical model of elastic wave propagation in porous media, we attempted as rigorous a quantitative assessment as possible of the natural gas present as gas hydrate above the BSR and as free gas between the BSR and the Base of Gas Reflector (BGR).

Key words: Bottom Simulating Reflectors, gas hydrates, natural gas, seismic tomography, South Shetland margin.

1 INTRODUCTION

Bottom Simulating Reflectors (BSRs) are broadly parallel to the sea floor in seismic reflection profiles and are believed to mark the pressure- and temperature-dependent base of the gas hydrate stability field in many geological settings (e.g. Markl *et al.* 1970; Shipley *et al.* 1979; Hyndman & Spence 1992). Analyses conducted on several active and passive margins where BSRs were found on seismic reflection records, in particular when aided by drilling, demonstrated that the reflectivity contrast is linked primarily to the low velocity associated with free gas trapped in the sediment pores below

the base of the gas hydrate stability zone (below the BSR on the seismic profile). Conversely, the presence of gas hydrates partially occupying the sediment pores in the hydrate stability zone may cause an increase (generally small) in the acoustic velocity above the base of the gas hydrate stability zone (above the BSR on the seismic profile), but no dramatic effect on sediment reflectivity as a result (Singh *et al.* 1993; Singh & Minshull 1994; MacKay *et al.* 1994; Holbrook *et al.* 1996; Andreassen *et al.* 1997; Tinivella & Lodolo 2000; Yuan *et al.* 1999). Besides the validation of seismic velocity data with borehole data, the relationships between amounts of natural gas in the clathrate-free pore space, and the resulting bulk

sediment compressional and shear wave velocity are supported by theoretical models (Wood *et al.* 1994; Lee *et al.* 1996; Tinivella 1999; Helgerud *et al.* 1999).

Studies conducted on the Peru Margin (Miller *et al.* 1991), in the vicinity of the Chile triple junction (Bangs *et al.* 1993), on the Cascadia Margin (MacKay *et al.* 1994), and in the three Blake Ridge drill holes (Ocean Drilling Program, Leg 164; Holbrook *et al.* 1996), have demonstrated that the thickness of the free-gas layer ranges from about 5 m, to <25 m, to ~50 m, to 250 m, respectively. These significant differences can often be explained by taking into consideration the intrinsic difficulties in detecting the base of the free gas zone with geophysical methods. Because of the typical frequency range (from approximately 5–50–60 Hz), conventional multichannel seismic reflection techniques are often unable to resolve the thickness of the free-gas layer below a threshold of about 10 m in the case of high-quality data. It follows that detection of the BSR, of the free-gas layer below it, and of the distribution of gas hydrates within the stability zone, depend heavily on the resolution of the seismic method employed.

In structurally complex areas, such as active continental margins, the geological factor becomes an additional fundamental variable in the recognition of the regional distribution of gas hydrates and associated free gas. This is because physical discontinuities in the upper crust, and deep over-pressurization of the pore fluids induced by tectonic overburden and stress, lead to an uneven distribution of fluids, varying heat flow, and varying physical properties of the geological formations. A clear dependence of the distribution of the BSR on the geological setting has been outlined for the Cascadia (Tréhu *et al.* 1999; Suess *et al.* 1999), Peru (Miller *et al.* 1991), Costa Rica (Pecher *et al.* 1998), and Aleutian margins (Suess *et al.* 1998).

In this paper we present a regional analysis of the distribution of the gas hydrates and free gas on the South Shetland margin (SSM, Fig. 1) based on the seismic evidence alone. An extensive multichannel seismic survey was conducted by the former Osservatorio Geofisico Sperimentale (OGS) in the frame of the Italian *Programma Nazionale di Ricerche in Antartide (PNRA)*, with the following main purposes; (a) to determine and map the extent of BSR on the SSM, (b) to reconstruct the compressional-wave velocity field associated with the BSR, (c) to image the BSR spatial geometry with respect to the sea floor, (d) to determine the relationships between the geological structure of the margin and the distribution of gas hydrate and free gas, and (e) to tentatively assess quantities of gas hydrates and free gas in the SSM using calculated acoustic velocities and theoretical velocity models.

In spite of the paucity of additional data (such as core samples, drilling data, seafloor observations and geochemical
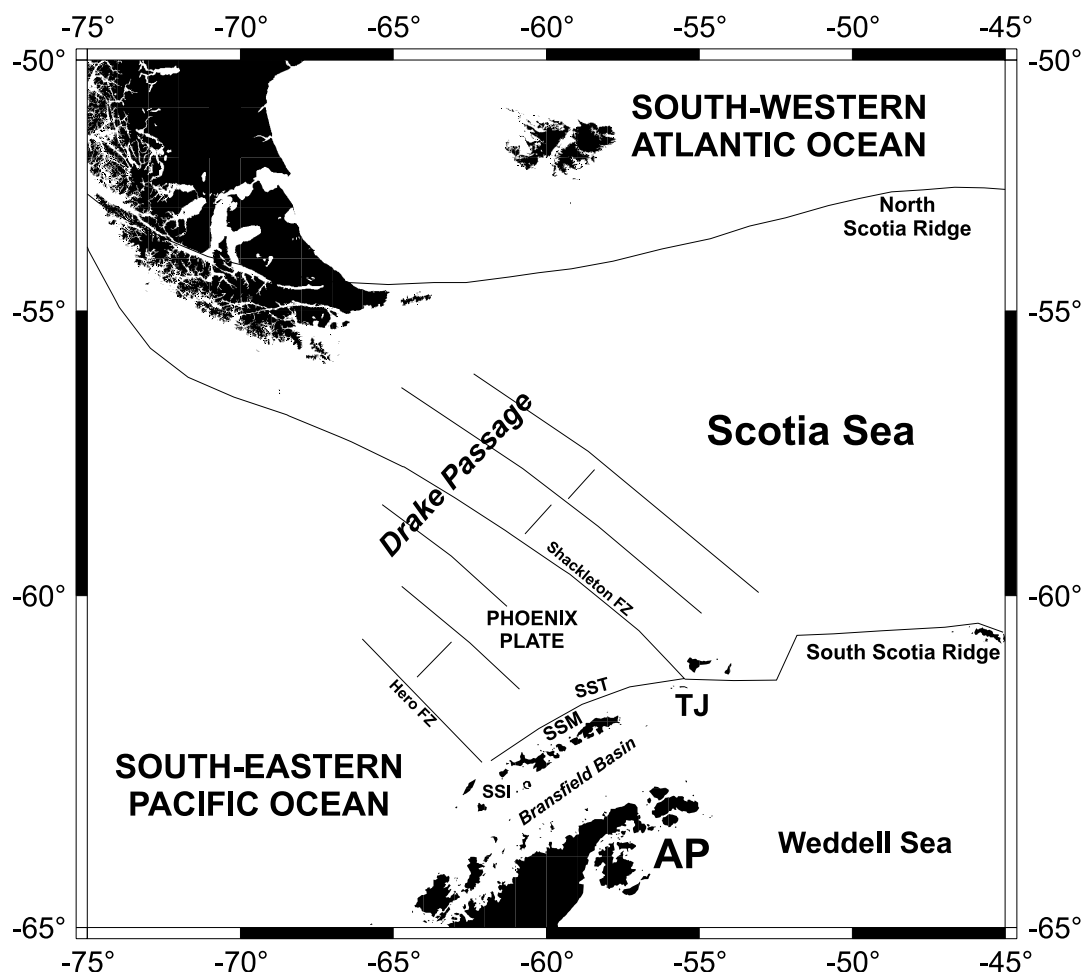

Figure 1. General tectonic map of the Scotia Sea region. SSI = South Shetland Islands; SSM = South Shetland Margin; SST = South Shetland trench; AP = Antarctic Peninsula; TJ = Triple Junction.

analyses in the water column), we have gathered conclusive evidence to assess provisionally the occurrence of free gas and gas hydrate in this convergent tectonic environment.

2 SEISMIC DATA ACQUISITION AND PROCESSING

A grid of about 750 km of GPS-fixed intermediate-resolution multichannel and single-channel seismic reflection profiles (Fig. 2), were acquired in February 1997 by the RV *OGS-Explora* on the SSM (Lodolo *et al.* 1998) using a 3000-m long analogue streamer with 120 channels (trace interval 25 m), and two GI-guns operated in harmonic mode (total volume 4 L) shooting every 25 m in order to obtain a 60-fold coverage. The record length is 7.0 s at 1 ms sampling rate. The conventional seismic processing applied to the data included; (1) re-sampling from 1 ms to 2 ms, (2) spherical divergence and absorption compensation, (3) trace editing and de-spiking, (4) normal-move-out and common-depth-point stacks, using stacking velocities derived from semblance-velocity-analyses, and constant-velocity-stacks (every 2 or 4 km), (5) deconvolution after stack, (6) three adjacent trace mixing and time-variant filtering, and (7) Kirchhoff time migration.

3 SOUTH SHETLAND CONTINENTAL MARGIN

3.1 Regional geological setting

The SSM occupies the NE part of the Pacific margin of the Antarctic Peninsula (Fig. 2). The margin represents the only remnant of the former Palaeozoic to Mesozoic Gondwanan subduction margin (de Wit 1977; Grunow *et al.* 1992), and presently marks the zone of convergence between the continental domain of the South Shetland platform and the oceanic crust of the Phoenix microplate. The long-term subduction history of the Pacific margin of the Antarctic Peninsula includes axial ridge crest–trench collisions that progressed from SW to NE, from the Eocene until the Pliocene, along the Pacific margin of the Antarctic Peninsula (Barker 1982; Larter & Barker 1991).

The South Shetland subduction zone is bounded by the Hero Fracture Zone to the SW, the Shackleton Fracture Zone to the NE, and the South Shetland trench to the SE. These three tectonic structures form triple junctions in which continental blocks and relatively young oceanic crust become part of a structurally complex geological environment (Klepeis & Lawver 1996; Aldaya & Maldonado 1996).
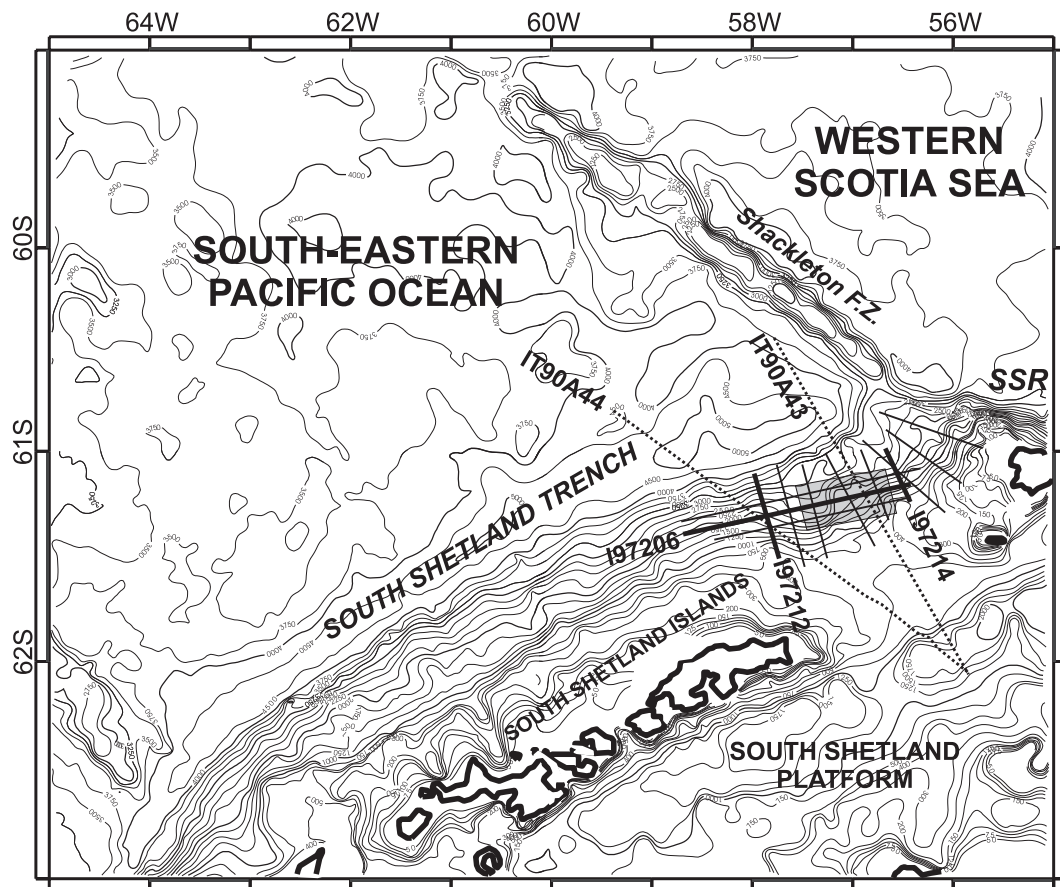

Figure 2. Bathymetric map of the South Shetland margin and part of the south-easternmost Pacific Ocean and western Scotia Sea, with location of the intermediate-resolution seismic grid acquired in 1997 and two low-resolution profiles acquired in 1989/90 (lines IT90A43 and IT90A44). Bathymetric measurements (all GPS-fixed) include data collected by the former Osservatorio Geofisico Sperimentale (OGS) during several Antarctic Campaigns, and by the British Antarctic Survey (BAS), and combined within the framework of the ANTOSTRAT Program (Cooper & Webb 1994). Thick lines indicate the three migrated profiles presented in Figs 5, 7 and 10. Grey box indicates the parts of the seismic lines where the tomographic analysis was performed. SSR = South Scotia Ridge.
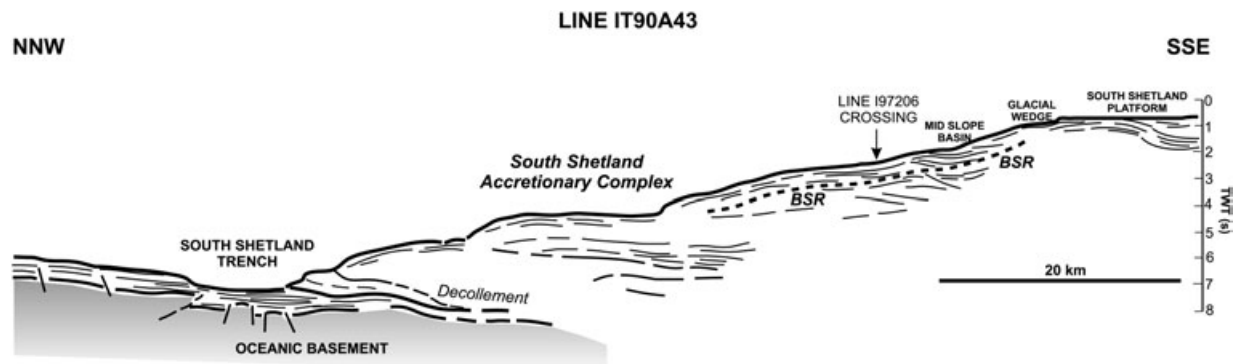
LINE IT90A43

Figure 3. Simplified line-drawing of part of the multichannel seismic profile IT90A43 acquired during the 1989/90 OGS Antarctic Campaign across the South Shetland margin, which exhibits the main morphostructural elements of this convergent margin. See Fig. 2 for location.

On a regional scale, we observe the coexistence of two different tectonic styles on the SSM, clearly related to distinct deformational regimes (Fig. 3). An older regime (Late Palaeozoic–Early Mesozoic to Middle Cenozoic) determined the gross structure of the present day SSM with building up of a subduction trench and accretionary prism with the development of thrust and reverse faults (Maldonado *et al.* 1994; Kim *et al.* 1995) as a consequence of the interaction between the Panthalassa oceanic lithosphere and the continental margin of the Antarctic Peninsula and southern South America. A younger tectonic style, superimposed on the older one, has produced mostly normal faults. This tectonic style was possibly related to the Late Miocene cessation of the seafloor spreading of the western Scotia ridge and subsequently of the Phoenix Ridge

(early Pliocene), with progressive reduction of ridge-push forces along these segments of the Antarctic margin. It caused the cessation of thrust faulting and folding, and the activation of the left-lateral Shackleton Fracture Zone and associated array of extensional faulting, approximately orthogonal to the strike-slip system.

The structural map in Fig. 4 shows that most of the extensional faults can be mapped with a strike roughly along slope, with the exception of one major fault (indicated as strike-slip fault in Fig. 4), with the largest vertical offset, which extends perpendicular to the margin, and subparallel to the Shackleton Fracture Zone. We interpret this lineament as a subsidiary fault of the Shackleton Fracture Zone and therefore as a sinistral strike-slip fault.
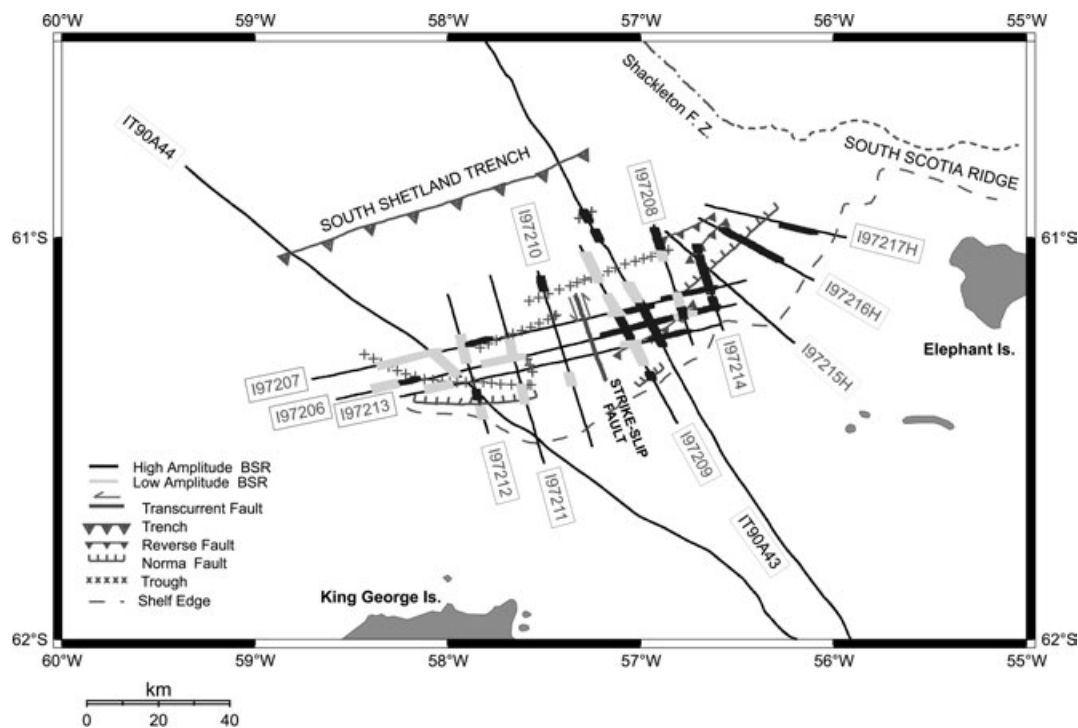

Figure 4. BSR distribution versus structural setting of the South Shetland continental margin, obtained from the interpretation of the whole available seismic dataset. The stronger BSR is mostly located to the east of a main strike-slip lineament (as imaged on seismic profile I97206), which bounds the highly tectonized area where the three principal elements of the Shackleton Fracture Zone, the South Scotia Ridge, and the South Shetland trench, mutually interact.
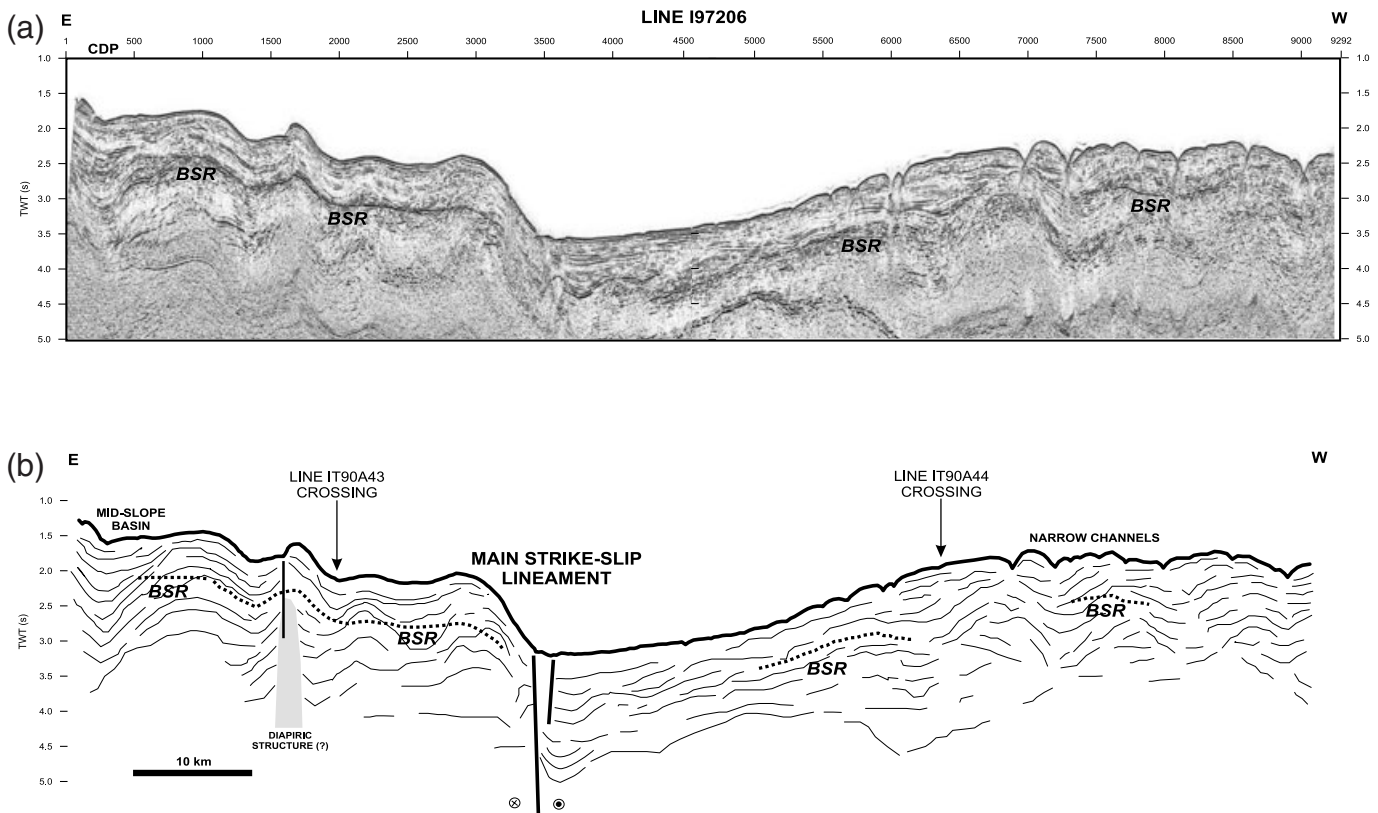
Figure 5. Migrated version (a) of seismic line I97206 (see Fig. 2 for location), which shows a prominent BSR on its eastern half, and which crosses folded structures without loss of strength. The western half of the profile, where the BSR continuity is not preserved, is characterized by sediment waves and erosive channels. A main strike-slip lineament, shown in the line drawing (b), separates the two areas where the structural architecture and the sedimentary setting are significantly different.

3.2 Sedimentary architecture

The structure of the margin (Fig. 3) is characterized by a gently dipping oceanic crust down-faulted to form horsts and grabens, onlapped by terrigenous sediments of the South Shetland trench (Maldonado *et al.* 1994; Kim *et al.* 1995; Camerlenghi *et al.* 1997). A wedge of accreted sediments is identified beneath the continental slope by an incoherent seismic response in which a chaotic configuration alternates with landward-dipping, high amplitude/low frequency reflectors. The dipping reflector produced by the top of the oceanic basalts is recognizable below the frontal thrust zone of the accretionary complex. The frontal thrust and the décollement can be followed up to 20 km landward of the deformation front. Mid-slope basins are common features, and are often bounded by extensional faults, which in some cases reach the sea floor. The upper part of the slope is represented by a prograding wedge of glacial sediments, characterized by frontal foresets and topsets beneath the continental shelf. We identified three sedimentary units in this margin: a deeper unit, intensely deformed and with a poor reflectivity, represents the oldest accreted terrane formed during the long history of Mesozoic–Cenozoic subduction and accretion along this margin. The unit shows evidence of reverse and thrust faulting and locally of anticlinal folding. The unit forms local basement highs, one of which is a possible shale diapiric structure (Fig. 5), which appear to have become inactive and were buried by recent sedimentation. A layered unit with extremely variable thickness ranging from 2 s to a few hundreds milliseconds two-way traveltime (twt) rests unconformably above

the first unit. The layered unit contains evidence of compressional deformation in the form of folding (Fig. 6), inherited from the deformation of the underlying accreted terranes. However, it is also dissected, probably in its latest phase of deposition,
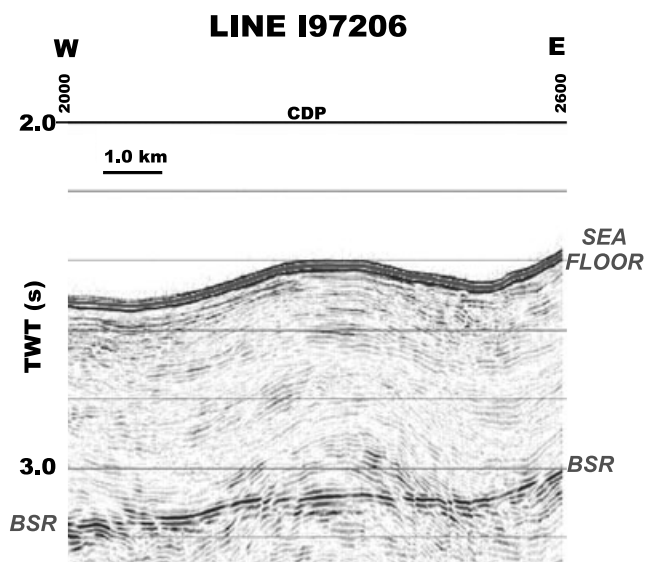

Figure 6. Part of the seismic profile I97206 where the BSR crosses an anticlinal fold. Note that the amplitude of the reflector is not significantly influenced by the presence of this structure, indicating that it does not affect the pressure-temperature stability field.

by extensional faults (Figs 7 and 8). This unit is topped by a deposit that is mostly basin-fill, with depocentres created by the activity of the extensional faults. This unit is most likely generated by the action of turbidity currents that originate on the upper slope from the progradation of a sedimentary wedge that downlaps on the underlying layered unit. Although no geological samples are available from this wedge, the geometry of progradation (steep foreset truncated by subhorizontal top-set on the continental shelf) and the anomalous water depth of the continental shelf, suggest that it is formed by the advances of a grounded ice shelf to reach the shelf break (see analogous examples from the neighbouring Pacific margin of the Antarctic Peninsula in Larter *et al.* 1997; or Rebesco *et al.* 1998). An extensive system of narrow channels dissects the
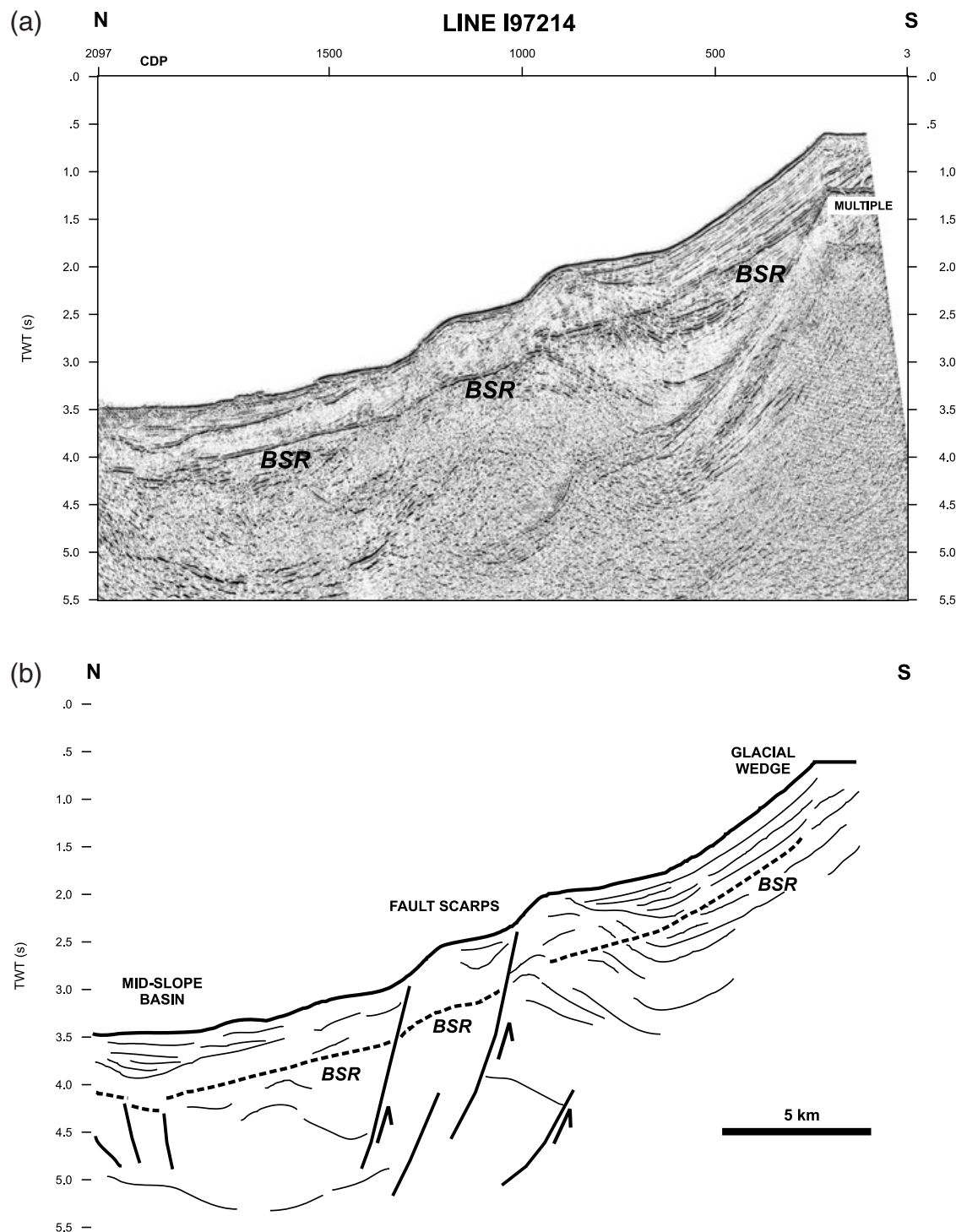

Figure 7. Migrated version (a) of seismic line I97214 (see Fig. 2 for location) and line-drawing (b), showing the BSR occurrence along the whole South Shetland margin continental slope, apart for localized areas where it is interrupted by fault systems (see Fig. 8) and basement structures (see Fig. 9).
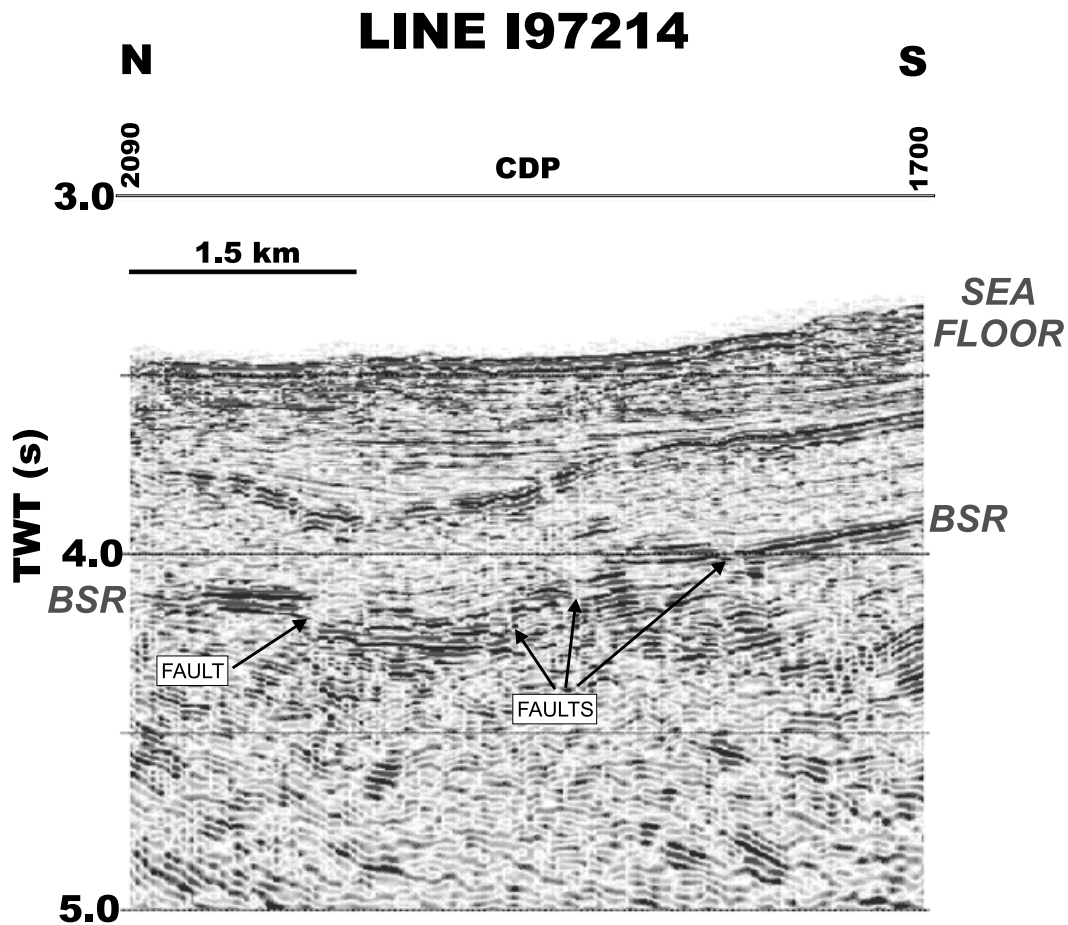
LINE I97214

Figure 8. Part of seismic profile I97214, where the BSR appears to be offset by a system of subvertical normal and reverse faults, coincident with the presence of a mid-slope basin.

uppermost sedimentary succession only, indicating a phase of syndepositional erosion, probably reflecting a late intensification of downslope sediment transport on this margin induced by glacial progradation (see Fig. 5).

3.3 Inferred sources of natural gas

There is no information from drilling regarding the litho-stratigraphy of the SSM, however, like the majority of the Antarctic margins, the source of terrigenous organic carbon (land vegetation) was eliminated as the climate cooled and ice sheets began to form. This cooling was associated with increased oceanic circulation and hence flux of marine biogenic sediments to the sea-floor, and presently the basins of Antarctica are filled with sediments which have relatively high concentrations of siliceous biogenic material (Anderson *et al.* 1983). The content of organic carbon is typically in the range of 1–3 per cent (Dunbar *et al.* 1985). These amounts are sufficient to transform organic debris to natural gases as a consequence of long-lived burial of organic matter under increasing temperature and pressure. Several DSDP and ODP sites in other regions of the Antarctic margins (Barker 1995 and reference therein; Barker *et al.* 1999) have demonstrated that sedimentation rates which accompanied the development of the ice sheets have been very rapid, on the order of tenths of metres per thousand years, thus contributing to a rapid burial history.

4 BSR DISTRIBUTION

The BSR (Fig. 9) is widespread in the NE sector of the SSM, in water depths ranging from 1000 to 4800 m. Sub-bottom two-way traveltime of the BSR generally varies between 500 ms at
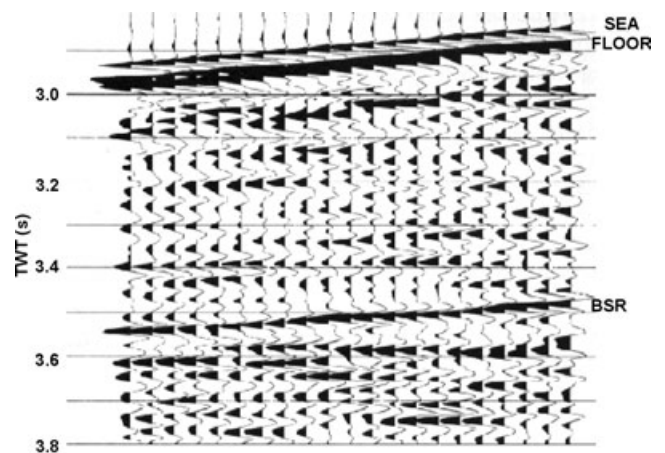

Figure 9. Display of some CDP traces of line IT90A43 (amplitude has been corrected for spherical divergence), showing the negative polarity of the BSR with respect to the sea floor reflection.

© 2002 RAS, *GJI* **148,** 103–119

the shallowest water depth and 900 ms at a depth of 4800 m in the vicinity of the South Shetland trench. The South Shetland margin BSR cuts across reflectors ranging from lower slope deformed accreted sediments, to slope basins, to deposits of the glacial wedge.

The BSR is superimposed on the sedimentary and structural configuration of the margin and crosses folded and deformed strata of the accreted terranes, but it is not particularly evident within the layered sequences of slope basin infill. The BSR crosses anticlinal folds without a significant loss in amplitude and strength (Fig. 6). The BSR is locally offset by extensional fault systems (Figs 7 and 8), while it seems to disappear at structural highs of the deeper unit (Fig. 10).

Amplitude and lateral continuity of the BSR vary significantly in the surveyed area. By superimposing the distribution of the BSR, and distinguishing its strength (high and low amplitude), on the structural map (Fig. 4), we observe that the main strike-slip fault clearly separates a zone to the east where the BSR is strong, generally continuous and characterized by a high amplitude, from a zone, to the west of the fault, where its strength is significantly reduced, it is difficult to detect and lacks continuity, as shown in Fig. 11, where it appears only occasionally at a mid-slope basin.

The area where the BSR is strongest is the triple junction between the Shackleton Fracture Zone, the South Shetland trench and the South Scotia Ridge. We found that a direct

relationship exists between abundance of gas hydrates and structural complexity, which may in some ways influence the movements of fluids responsible for free-gas accumulations and gas-hydrate formation. In this study this relationship is not supported by direct observations of fluid advection along the faults, but the fact that faults act as important conduits for the focusing of fluids (water and gas) and heat, which obviously must disturb BSRs, is demonstrated unequivocally by several multidisciplinary studies of convergent margins (Pecher *et al.* 1998; Tréhu *et al.* 1999; Ruppel & Kinoshita 2000; among others). On the contrary, in areas dominated by ductile deformation (synclinal and anticlinal folds), the BSR continuity is preserved and the reflector's amplitude does not vary significantly. This suggests that the stratigraphic configuration and deformed sequences do not affect the temperature–pressure stability field for gas-hydrate formation. The occurrence and strength of the BSR does not appear to depend on the lithology of the sediments. The BSR is observed within the accreted terranes, within the layers of sedimentary units and within the glacial wedge on the upper continental slope. The apparent occasional absence of the BSR can be explained by: (1) the destructive interference between the BSR and the high-amplitude, and subparallel to the sea-floor, sedimentary reflectors of the slope basin sequences, and (2) the absence of a negative contrast in acoustic impedance at the base of the gas-hydrate stability zone. This is generally interpreted as
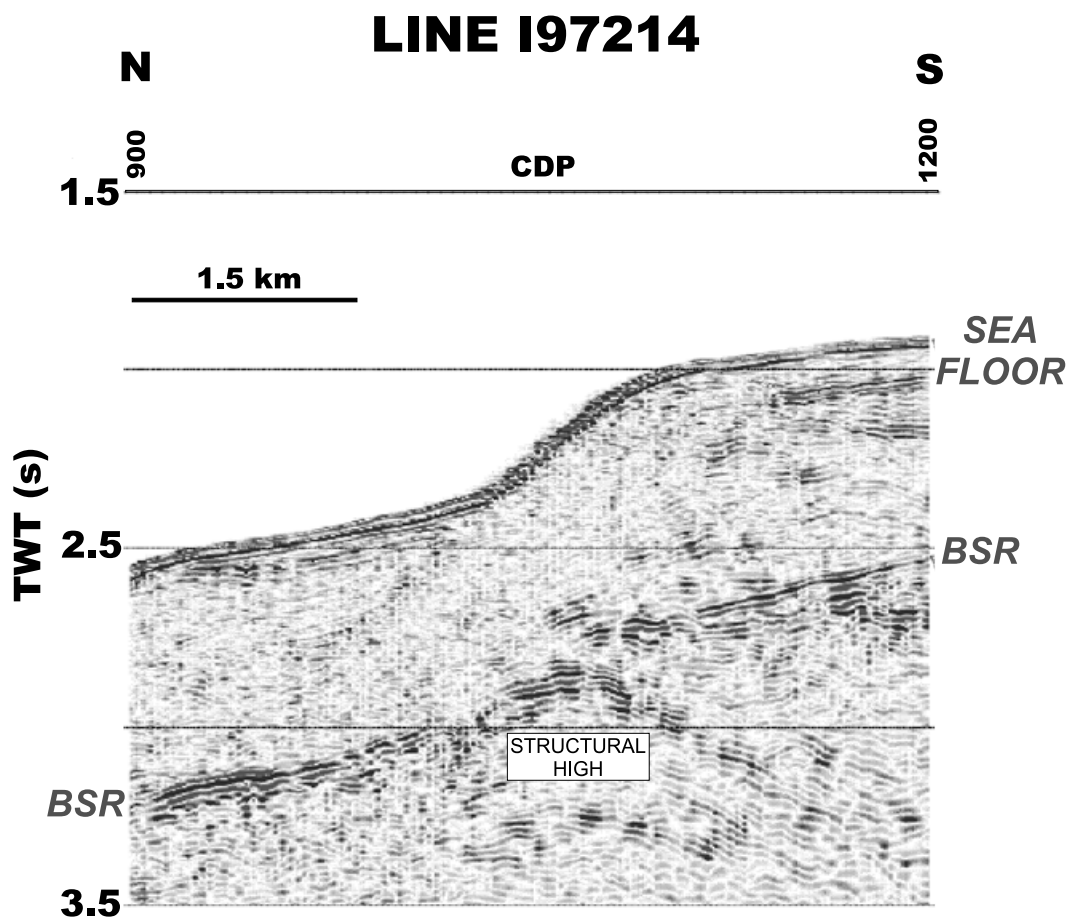

Figure 10. Interference between a structural high in the basement and the BSR along part of line I97214; the BSR disappears over the top of the structure.
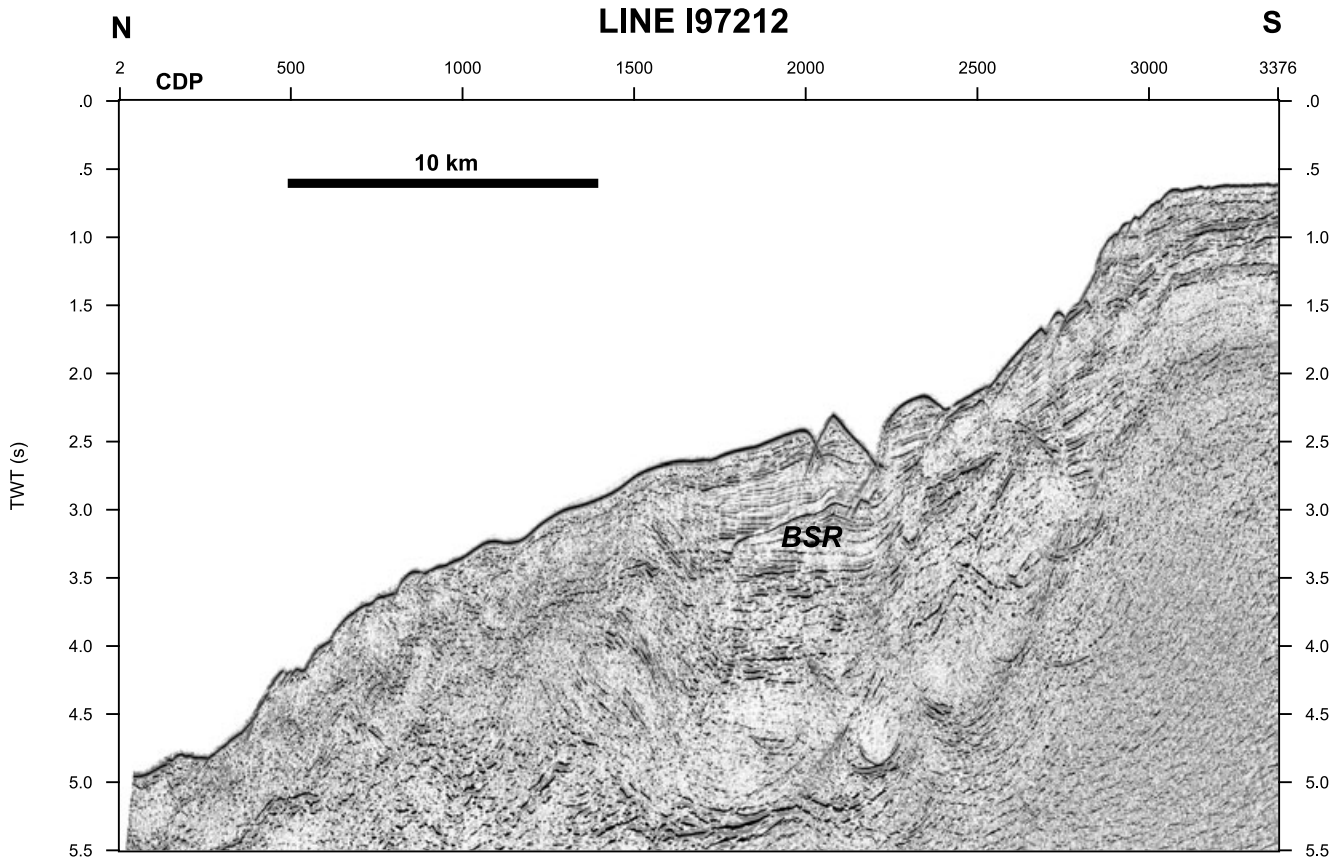
Figure 11. Migrated version of seismic line I97212 (see Fig. 2 for location). In this profile, the appearance of the BSR is discontinuous, apart from the central part of the slope, where two main structural breaks are present.

the absence of free natural gas trapped below the gas hydrate seal, but not necessarily as the absence of gas hydrates in the sedimentary section, as demonstrated by drilling in the Blake Ridge (ODP Leg 164; Paull *et al.* 2000).

5 FREE GAS BELOW THE GAS HYDRATE STABILITY ZONE

One particular aspect of the BSRs of the SSM is that on low-resolution multichannel seismic reflection profiles, a normal polarity reflector is often present a short distance below, and subparallel to, the BSR, which identifies the base of the gas layer (BGR = Base of Gas Reflector; Böhm *et al.* 1995; Tinivella *et al.* 1998). The presence of gas below the BSR was tested through tomographic inversion of traveltimes, which revealed a negative velocity anomaly with respect to a normally compacted marine terrigenous sequences at the same sub-bottom depth (Hamilton 1978). Velocity is as low as 1300 m s^{-1} between BSR and BGR. The thickness of the free-gas zone was estimated on average to be about 50 m, with local increases of as much as 400 m.

The dedicated survey carried out in 1997 using a lower energy, but higher frequency, source (two G.I. guns, total volume of 4 L) compared to the earlier survey of 1989/90 (Lodolo *et al.* 1993), where 2 tuned arrays of 15 Bolt guns each (total volume of 45 L), were deployed, did not provide clearer evidence of the BGR. On the contrary, the BGR is less visible on the higher resolution stacked and migrated sections, appearing occasionally, and not necessarily where the BSR is stronger.

A study conducted on the velocity structure through the BSR of the SSM on profile I97206 using both reflected and refracted rays (Tinivella & Accaino 2000) shows that: (1) the BGR becomes visible, at least in the single location where the Ocean Bottom Seismometer (OBS) study was conducted, if a dedicated and detailed velocity analysis is performed, via tomographic inversion of refracted and reflected arrivals, and pre-stack depth migration is applied (see their Fig. 6); (2) the velocity inversion between BSR and BGR is detected by reflected rays, but the velocity field within the gas layer is highly variable; (3) an additional reflector between BSR and BGR is present, which probably indicates a level of different gas concentration within the free-gas layer.

We have compared the pre-stack reflected wavelets of the low- and intermediate-resolution data at the crossing point between profiles IT90A43 and I97206, respectively, which occurs where the BGR is easily visible on the low-resolution data (Fig. 12). The reflection of the base of the gas layer is present before the stack in both datasets. The higher energy of the low-resolution surveys makes it a higher amplitude reflector, so that during the stacking procedure it survives the stacking and migration of the noise produced by the rough geological structure, which implies a highly variable velocity field. Conversely, the lower amplitude reflector of the higher resolution survey is lost in the background geological reflectors unless the velocity is better constrained for stacking and migration. Additionally, we consider the possibility that a gradual change of gas concentration occurs towards the base of the gas layer, so that it is better reflected by a longer wavelength pulse.
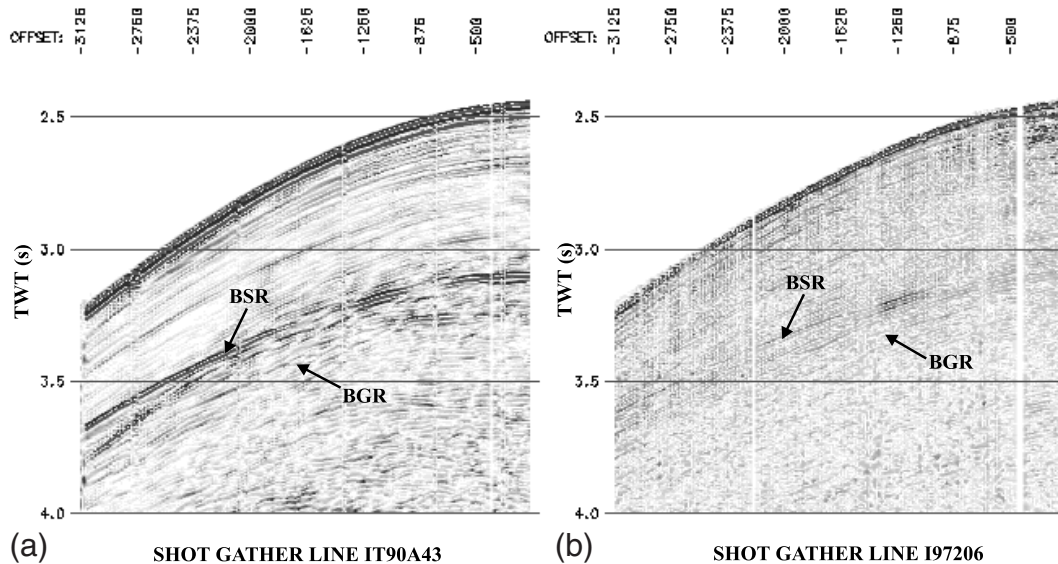
Figure 12. Two examples of shot gathers taken at the crossing point between the low-resolution seismic profile IT90A43 (a), and intermediate-resolution profile I97206 (b). Note the different appearance of the BSR and BGR in the two datasets (see text for details).

6 ACOUSTIC VELOCITY STRUCTURE AND SPATIAL GEOMETRY OF THE BSR

Following the mapping of the occurrence and strength of the BSR on the grid of seismic profiles, we proceeded to a velocity analysis aimed at the recognition of the gas hydrate and free gas zones. The conventional processing methods to estimate the interval acoustic velocity from seismic data (i.e. semblance-velocity-analyses and constant-velocity-stack analyses) furnish only a gross distribution of the velocity structure because of the spatial average carried out over the acquisition spread, which is 2670 m in our case. Moreover, the stacking velocity spectra method (Taner & Köhler 1969) assumes a very crude model for the Earth (i.e. homogeneous horizontal layers), and neglects ray bending at the layer interfaces due to Snell's law. Tomographic inversion of traveltimes allows a better definition of lateral velocity gradients, than do semblance analyses, and a better control on the intervals over which the analysis is performed (e.g. Worthington 1984; Nolet 1987; Stewart 1991; Carrion *et al.* 1993a, 1993b). Moreover, it allows the estimation of seismic velocity in depth for any combination of source and receiver position. In particular, the method used here implies the discretization of a continuum into a certain number of layers, separated by curved interfaces defined by bi-cubic splines (Böhm *et al.* 1999) and subdivided in parallelepipeds, the sections of which may be a regular or irregular polygons (Böhm, Galuppo & Vesnaver 2000). The ray tracing is based on Fermat's principle (Vesnaver 1994, 1996a, 1996b; Böhm *et al.* 1999), while for the inversion, the Simultaneous Iterative Reconstruction Procedure (SIRT) method is adopted (Van der Sluis & Van der Vorst 1987; Stewart 1991).

Reflectors are picked manually on the data before stack, in both common offset and shot gathers, using a limited number of traces where the amplitude contrasts of the selected horizons are larger. The inversion procedure begins with an initial arbitrary velocity model both for velocities and depths of the reflectors. An iterative loop allows us to automatically invert both the velocity distribution and the geometry of the reflectors considered (Rossi & Vesnaver 1997). At each step of the loop,

the time residuals converted into depth residuals are checked, and the iterative procedure stops when their dispersion around the fitted reflector reaches a minimum. An analogous method has been applied to small parts of seismic reflection profiles containing a BSR on the SSM (Tinivella *et al.* 1998) and on the Blake Ridge (Tinivella & Lodolo 2000), with the main purpose of defining the free-gas layer below the BSR.

In the present case, we applied the tomographic inversion to a larger data set, formed by a selection of intermediate-resolution seismic profiles collected in 1997 on which the BSR was mapped as strong and continuous (see in Fig. 2 the location where BSR tomography analysis was performed). 25700 traces with offset from 130 to 2000 m were selected for picking of two horizons only, the sea-floor, and the BSR, in order to image the 3-D distribution of the BSR with respect to the sea-floor. Initially, a dense regular grid of pixels was used. However, the elevated number of pixels allows for an uneven distribution of the rays with respect to the seismic grid, and therefore the generation of null space. Subsequently, a lower number of larger pixels was adopted, with the advantage of increasing the reliability of the solutions, in spite of the lower local resolution. As a final step we adapted the grid by assigning irregular shapes to the pixels (Voronoi polygons) in such a way that the space has been discretized depending on the velocity field and on the null space with an automated code. Pixels are smaller where the density of rays is larger and vice versa (Böhm, Galuppo & Vesnaver 2000).

As a result of the tomographic inversion, a map of the depth of the sea-floor, of the BSR, and of the distribution of the averaged velocity values above, is produced (Fig. 13). The BSR varies from a depth of about 1700 m to about 2800 m, following and exaggerating the wedge topography and showing increasing depths seaward. On the continental shelf the BSR is not present, and this explains the apparent greater depth in this zone. The velocity distribution is not uniform on the area. Local increments may be associated either with the local abundance of gas hydrates or with high-velocity layers (deformed accreted sediments between sea floor and the BSR). Local reductions of interval velocity that do not correspond to loss of
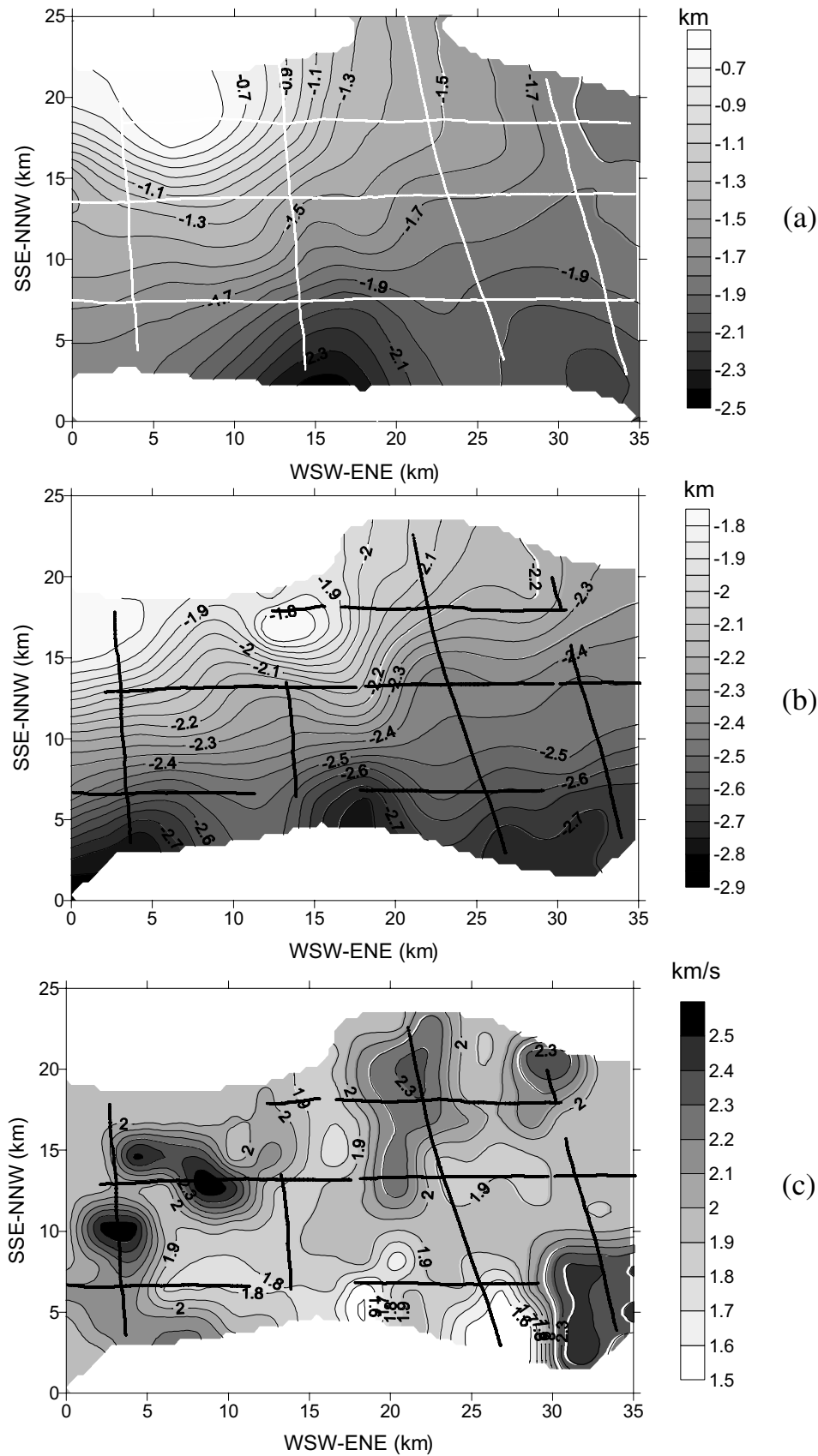
Figure 13. Results of the inversion of traveltimes in the area to the east of the main structural lineament identified on line I97206 where a strong BSR was found (see box in Fig. 2 for location). The calculation has been performed on an area of 25×35 km. Panel (a) shows the geometry of the sea floor (contours in km); panel (b) shows the geometry of the BSR (contours in km); panel (c) shows the average compressional velocity field above the BSR interface (contours in km s^{-1}).

BSR strength testify that the appearance of the BSR reflector is not inevitably associated with the presence of gas hydrate above the gas hydrate stability zone, but is mostly due to the free-gas zone present below.

7 SOUTH SHETLAND MARGIN RESERVOIR POTENTIAL

The determination of the quantities of gas hydrates and free gas trapped in marine sedimentary sequences requires a method in which the differences between an experimental velocity curve (in our case, the experimental velocity field is that obtained from the application of the seismic tomography method) and a given theoretical velocity function (in our case an empirical curve) can be transferred into concentrations of gas hydrates and free gas in the sediment pores.

We use the approach of Domenico (1977) to model the acoustic properties of different layers associated with the BSR (Tinivella 1999; Tinivella & Lodolo 2000). This method includes an explicit dependence on differential pressure and depth, and it takes into account the effects of cementation by gas hydrates on the shear modulus of the sediment matrix. Moreover, it is possible to model the transition between low (no cementation) and high (cementation) gas hydrate concentration. The theory provides equations for both compressional and shear wave velocities as functions of a number of physical parameters, such as porosity, compressibility, rigidity, density and frequency dependence. These parameters are determined from available lithostratigraphic information, downhole and core logging (if present) and/or general experimental data sets, such as Hamilton's curves (Hamilton 1978). The models permit the coexistence of two solid phases (grains and clathrates), and two fluid phases (water and free gas).

According to Domenico (1977), the compressional wave velocity is expressed as (see explanation of symbols and variations of material properties versus depth in Table 1):

$$V_p = \left\{ \left[\left(\frac{1}{C_m} + \frac{4}{3}\mu \right) + \frac{\frac{\phi_{eff}\rho_m}{k\rho_f} + \left(1 - \beta - 2\frac{\phi_{eff}}{k}\right)(1-\beta)}{(1-\phi_{eff}-\beta)C_b + \phi_{eff}C_f} \right] \times \frac{1}{\rho_m \left(1 - \frac{\phi_{eff}\rho_f}{k\rho_m}\right)} \right\}^{1/2} \quad (1)$$

This equation can be applied in the case of: (1) full water saturation (to reproduce the absence of gas in either the hydrated or gaseous phase) (2) water and gas hydrates in the pore space, and (3) water and free gas in the pore space. The composite fluid and solid compressibilities are considered to be Hill's average between the Voigt and Reuss averages (Schön 1996), while the pore compressibility is derived from an empirical function for pore volume (Domenico 1977). The effect of grain cementation, when the concentration of gas hydrates is high, is considered by application of the percolation model (Leclaire 1992), which describes the transition of a two-phase system from a continuous (100 per cent grain cementation) to a discontinuous (no cementation) state. Finally, it is worth mentioning that the coupling factor k describes the degree of coupling between pore fluid and solid frame. Numerically, it ranges from one to infinity and is a function of the frequency of the elastic wave considered.

The concentrations are estimated by fitting the theoretical velocity (eq. 1 above) to the experimental P-wave velocity obtained from traveltime inversion. If the local geological setting is simple, the discrepancies between the inverted velocity profile and the predicted velocity for water-filled normally compacted marine sediments are interpreted to be due to the presence of gas hydrate (where positive anomalies are present) and free gas (where negative anomalies are present). The method has been tested against sonic log data and indirect estimations of gas hydrate concentrations from chloride content of the pore waters at ODP Leg 164 drill sites (Paull *et al.* 2000; Tinivella 1999; Tinivella & Lodolo 2000). If the geological setting is complex, such as in the case of the SSM (Tinivella *et al.* 1998), the interpretation of results must take into consideration the possibility that positive velocity anomalies could be produced by lithological changes, sediment deformation, and diagenetic alteration.

We performed a quantitative assessment of gas hydrates and free gas in the area covered by the seismic grid, which includes as much information as possible obtained by the analysis of multichannel seismic reflection profiles and OBS refraction data available on this margin. The procedure was as follows:

(1) We identified type seismic sections of the high amplitude and low amplitude BSR mapped in the area. These are: profile IT90A44 for the weak BSR (6 km of data were considered for the analysis), and profiles IT90A43 and I97206 for the strong BSR (21.5 and 20 km of data considered, respectively).

(2) Acoustic tomographic inversion of reflected traveltimes (including refracted traveltimes on profile I97206) were considered according to the work presented by Tinivella *et al.* (1998) and Tinivella & Accaino (2000). Velocity profiles were obtained by sampling the velocity field every 500 m, then averaging along each reflection profile, and subsequently for each BSR strength zone (Fig. 14a,b). Note that the velocity anomaly in the upper 100 m is not reliable and is probably due to picking errors in the vicinity of the seafloor. The anomaly in the upper 100 m will be neglected in subsequent calculations.

(3) Two profiles of the concentration (volume occupancy) of gas hydrates above the BSR and free gas between the BSR and the BGR were obtained (Figs 14c.d) by comparing the two type velocity profiles with Hamilton's velocity profile in terrigenous sediments (Hamilton 1978) using the procedure described in Tinivella (1999). The two type sections reveal that free gas is present in low concentrations in both settings. However, the gas concentrations are higher where the BSR is stronger, as expected. On the contrary, a slightly higher concentration of gas hydrates is modelled in the weak BSR area, which is not evident in the seismic record (it does not cause seismic reflectors and it does not affect the signal amplitude).

(4) The profiles of concentrations were extrapolated areally over the zones mapped as strong and weak BSR accordingly.

(5) The amounts of natural gas potentially derived from dissociation of gas hydrates and from free gas have been calculated at standard conditions of pressure and temperature, which yields 164 m^3 of free gas derived from 1 m^3 of gas hydrate, and 282 m^3 derived from 1 m^3 of natural gas. From the calculations for the part of the SSM where the BSR is mapped we obtained an amount of 2.3×10^{12} m^3 for natural gas

Table 1 List of parameters in eq. (1) and variation of material properties versus depth (after Tinivella 1999)

Parameter	Meaning	Value
$[z]=$ km	Depth below see bottom	
ϕ	Porosity	0.4–$0.45z+0.5z^2$
ϕ_0	Porosity at the sea bottom	0.4
ϕ_s	Solid proportion	
ϕ_h	Gas hydrate proportion	
ϕ_w	Water proportion	
ϕ_g	Free gas proportion	
$\phi_s+\phi_w+\phi_g=1$		
$\phi_s+\phi_h+\phi_w=1$		
$c_h=\phi_h/(\phi_h+\phi_w)$	Gas hydrate concentration	
$s_s=\phi_s/(\phi_{hs}+\phi_h)$	Grain saturation	
$s_h=\phi_h/(\phi_h+\phi_s)$	Gas hydrate saturation	
$s_w=\phi_w/(\phi_w+\phi_g)$	Water saturation	
$s_g=\phi_g/(\phi_w+\phi_g)$	Free gas saturation	
$\phi_{eff}=(1-c_h)\phi$	Effective porosity	
C_s	Grain compressibility	0.027 (GPa)$^{-1}$
C_h	Gas hydrate compressibility	0.119 (GPa)$^{-1}$
p	Hydrostatic pressure	Pa
C_w	Water compressibility	$4.631e^{-10}-9.5e^{-15}p$ Pa
C_g	Free gas compressibility	42.4 (GPa)$^{-1}$
C_b	Average compressibility of the solid phase	Pa^{-1} Hill's average (Schön 1996)
C_f	Average compressibility of the fluid phase	Pa^{-1} Hill's average (Schön 1996)
p_d	Differential pressure	Pa
$C_p=(1-\phi/\phi_0)/p_d$	Pore compressibility	Pa^{-1}
$C_m=(1-\phi_{eff})C_b+\phi_{eff}C_p$	Compressibility of the matrix	Pa^{-1}
$\beta=C_b/C_m$		
ρ_s	Grain density	2650 kg m^{-3}
ρ_h	Gas hydrate density	920 kg m^{-3}
ρ_w	Water density	Fofonoff & Millard (1985)
ρ_g	Gas density	88.48 kg m^{-3}
$\rho_b=s_s\rho_s+s_h\rho_h$	Density of the solid phase	kg m^{-3}
$\rho_f=s_w\rho_w+s_g\rho_g$	Density of the fluid phase	kg m^{-3}
$\rho_b=(1-\phi_{eff})\rho_b+\phi_{eff}\rho_f$	Average density	kg m^{-3}
Versus	Shear wave velocity	m /s Hamilton (1976)
$\mu_{sm0}=\rho_b(\text{Versus})^2$	Solid matrix shear modulus (no cementation)	Pa
μ_{smKT}	Kuster and Toksöz's shear modulus	Pa Kuster & Toksöz (1974)
$\mu_{sm}=(\mu_{smKT}-\mu_{sm0})[\phi_h/(1-\phi_s)]^{3.8}+\mu_{sm0}$	Solid matrix shear modulus	Pa
$\mu_s=\mu_{sm}/(1-\phi)$	Grain rigidity	Pa
μ_h	Gas hydrate rigidity	3.7 GPa
$\mu=(\phi_s+\phi_h)(\phi_s s_s/\mu_{sm}+s_h/\mu_h)^{-1}$	Average rigidity of the skeleton	Pa
k	Coupling factor	$1=k=\infty$

derived from the gas hydrate layer, and 5.9×10^{10} m^3 for free gas located below the BSR (Table 2). It is assumed that free gas distribution is quite uniform in the pore space. It is interesting to note that in this reservoir, where free gas layers are widespread and of significant thickness, the amount of free gas trapped beneath the gas hydrate layer is about two orders of magnitude less than the natural gas stored as the hydrate phase.

We cannot produce reliable estimates of the uncertainties of these volume calculations, because these depend on the numerical value of a large number of parameters (see Table 1), most of which are not measured (with an associated error) but are assumed from literature.

These values may be tentatively compared with global estimates of total natural gas trapped in and beneath gas hydrate reservoirs proposed by several authors (see the reviews by Kvenvolden 1998; Haq 1998), although these values vary significantly (by at least one order of magnitude) as a consequence of the diverse assumptions considered in the calculations. Accepting the value of 2–4×10^{16} m^3 proposed by Kvenvolden (1998) as a global reservoir of methane gas from gas hydrate layers, our estimate of the SSM represents $1/10000$ of the global estimate and it is about twice that estimated in the Prudhoe-Kuparuk oil field, Alaska (Collett 1992), and one order of magnitude less than the Bering Sea reservoir (Scholl & Hart
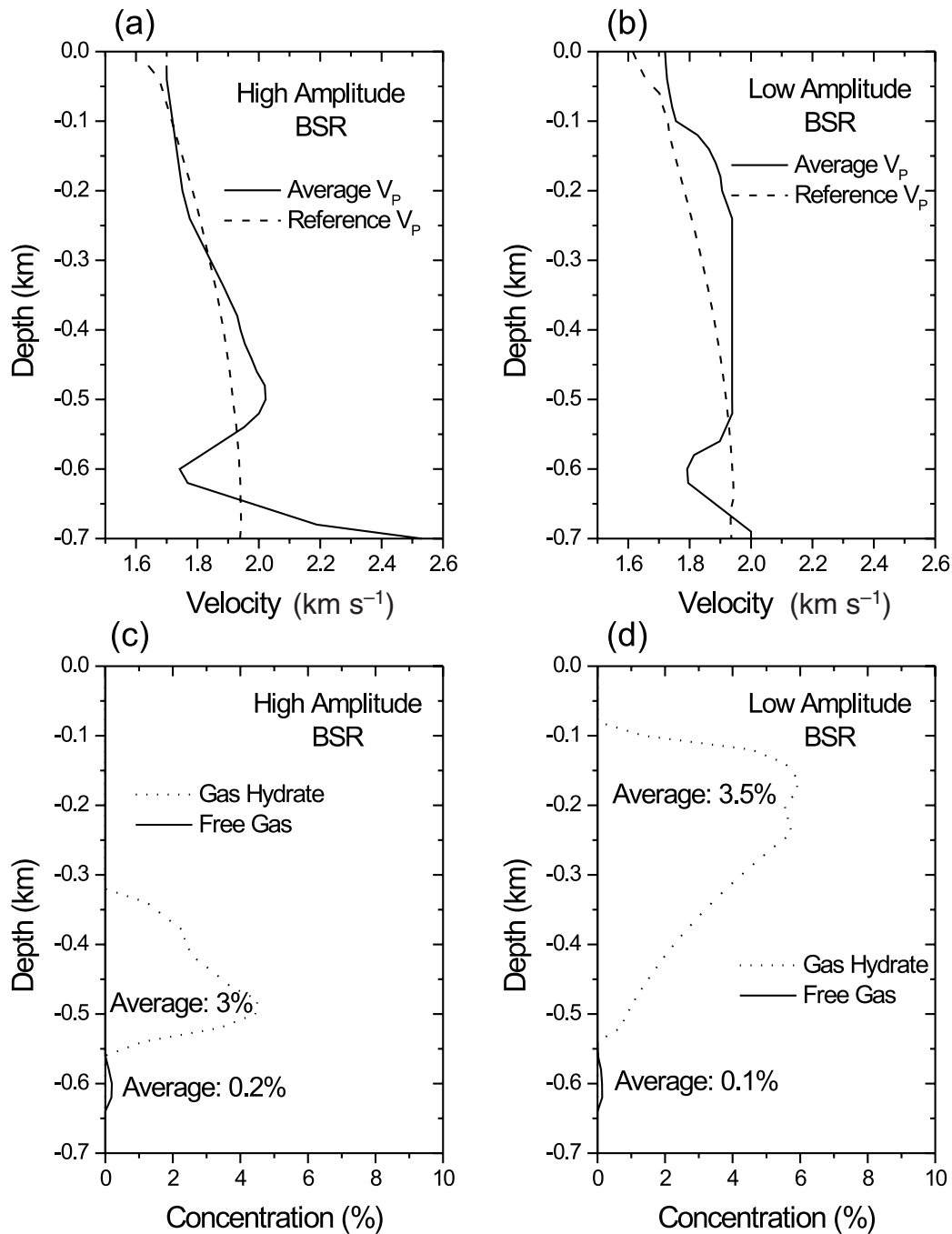
Figure 14. Curves of the *P*-wave acoustic velocities obtained from seismic tomography, in the case of a high-amplitude BSR (a) and a low-amplitude BSR (b). The dashed curve indicates the reference velocity function for normally compacted marine sediments. Panels (c) and (d) show the concentrations of gas hydrate and free gas for the cases of high- and low-amplitude BSRs, respectively.

1997), which extends however, over an area much larger than the SSM reservoir.

8 CONCLUSIONS

The results obtained from the analysis conducted on the intermediate-resolution multichannel seismic reflection lines collected across the SSM can be summarized as follow:

(1) The margin is characterized by two distinct, superimposed structural settings. An older one, which resembles mainly compressional structures generated by the long–term interaction between the Panthalassa oceanic crust and the Gondwana margin, and a younger one, where the tectonism is principally related to extensional stress fields, and associated with the Late Tertiary development of the western Scotia Sea.

(2) The BSR occurs, discontinuously, on the NE sector of the SSM, in water depths ranging from 1000 to 4800 m. Its strength varies significantly. On a regional scale, BSR amplitudes are higher where the geological structure is more complex, and lower where no significant structural discontinuities are present.

Table 2 Values used to estimate the natural gas potential in the South Shetland margin

	High amplitude BSR	Low amplitude BSR
Extent of the BSR	924 km^2	438 km^2
Average porosity in the gas hydrate zone	40 per cent	40 per cent
Average thickness in the gas hydrate zone	250 m	200 m
Average porosity in the free gas zone	35 per cent	35 per cent
Average thickness in the free gas zone	90 m	90 m
Average concentration of gas hydrate in the pore space	3 per cent	3.5 per cent
Average concentration of free gas in the pore space	0.2 per cent	0.1 per cent
Amount of natural gas from gas hydrates	1.2×10^{12} m^3	1.1×10^{12} m^3
Amount of free gas	4.8×10^{10} m^3	1.1×10^{10} m^3
TOTAL	1.25×10^{12} m^3	1.11×10^{12} m^3

(3) Seismic data show that the BSR offsets correspond to main discontinuities and faults, whereas the existing stratigraphic setting and the presence of folded structures do not significantly influence the BSR's strength. Our interpretation is that fault structures act as preferential conduits for the migration of fluids towards the surface, causing disturbances at the base of the gas hydrate stability field.

(4) The Base of Gas Reflector (BGR) is less visible on this data set than on previous low-resolution seismic profiles acquired in the same area, probably because of a combination of factors due to the lower energy source of the higher resolution survey and the transitional character of the base of the gas layer which makes it more reflective if surveyed with longer wavelength pulses.

(5) The reflection tomography method adopted for reconstructing the compressional-wave velocity field between the sea floor and the BSR horizon has allowed us to produce a map of the depth of the BSR.

(6) By modelling the acoustic parameters of the hydrate bearing and free gas bearing sediments, an average distribution of natural gases has been obtained and converted into concentrations of natural gas. The resulting potential of the SSM as a reservoir, is about 2.36×10^{12} m^3 of natural gas, stored both in gas hydrates and as free gas.

ACKNOWLEDGMENTS

REFERENCES

Aldaya, F. & Maldonado, A., 1996. Tectonics of the triple junction at the southern end of the Shackleton Fracture Zone (Antarctic Peninsula), *Geo-Mar. Lett.,* **16,** 279–286.

Anderson, J.B., Brake, C., Domack, E.W., Myers, N.C. & Wright, R., 1983. Sedimentary Dynamics of the Antarctic Continental Shelf, in: *Antarctic Earth Sciences,* pp. 387–389, eds R.L. Oliver, P.R. James & J.B. Jago, Australian Academy of Science, Canberra.

Andreassen, K., Hart, P.E. & McKay, M., 1997. Amplitude versus offset modeling of the bottom simulating reflection associated with submarine gas hydrates, *Mar. Geol,* **137,** 25–40.

Bangs, N.L.B., Sawyer, D.S. & Golovchenko, X., 1993. Free gas at the base of the gas hydrate zone in the vicinity of the Chile triple junction, *Geology,* **21,** 905–908.

Barker, P.F., 1982. The Cenozoic subduction history of the Pacific margin of the Antarctic Peninsula: ridge crest–trench interaction, *Journal of Geol. Soc. London,* **139,** 787–801.

Barker, P.F., 1995. The proximal marine sediment record of Antarctic climate since the Late Miocene. In: *Geology and Seismic Stratigraphy of the Antarctic Margin,* pp. 25–57, eds Cooper, A.K., Barker, P.F. & Brancolini, G., American Geophysical Union, Washington DC.

Barker, P.F., Camerlenghi, A., Acton, G.D. *et al.*, 1999. *Proceedings of the ODP, Init. Repts., 178.* ODP Texas A & M University, College Station, 77845–79547, CD-ROM.

Böhm, G., Camerlenghi, A., Lodolo, E. & Vesnaver, A., 1995. Tomographic analysis and geological contex of a bottom simulating reflector on the South Shetland Margin (Antarctic Peninsula), *Boll. Geof. Teor. Appl.,* **37,** 3–23.

Böhm, G., Galuppo, P. & Vesnaver, A., 2000. 3-D adaptive tomography by Delaunay triangles and Voronoi poligons, *Geophs. Prosp.,* **48,** 723–744.

Böhm, G., Rossi, G. & Vesnaver, A., 1999. Minimum-time ray-tracing for 3-D irregular grids, *J. Seismic Explor.,* **8,** 117–131.

Camerlenghi, A., Crise, A., Pudsey, C.J., Accerboni, E., Laterza, R. & Rebesco, M., 1997. Ten-month observation of the bottom current regime across a sediment drif of the Pacific margin of the Antarctic Peninsula, *Antarctic Sci.,* **9,** 424–431.

Carrion, P., Böhm, G., Marchetti, A., Pettenati, F. & Vesnaver, A., 1993a. Reconstruction of lateral gradients from reflection tomography, *J. Seismic Explor.,* **2,** 55–67.

Carrion, P., Vesnaver, A., Böhm, G. & Pettenati, F., 1993b. Aperture compensation tomography, *Geophysical Prospecting,* **41,** 367–380.

Collett, T., 1992. Potential of has hydrates outlined, *Oil Gas J.,* **90,** 84–87.

Cooper, A.K. & Webb, P.N., 1994. The ANTOSTRAT Project: An international effort to investigate Cenozoic Antarctic glacial history, climates, and sea level changes, *Terra Antartica, Spec. Issue,* **1,** 239–242.

Domenico, S.N., 1977. Elastic properties of unconsolidated porous sand reservoirs, *Geophysics,* **42,** 1339–1368.

Dunbar, R.B., Anderson, J.B., Domack, E.W. & Jacobs, S.S., 1985. Oceanographic influences on sedimentation along the Antarctic continental shelf, *AGU. Antarctic Res. Series,* **43,** 291–312.

Fofonoff, N.P. & Millard, R.C. Jr, 1985. *Technical Papers in Marine Science,* 44, UNESCO, Paris.

Grunow, A.M., Dalziel, I.W.D., Harrison, T.M. & Heizler, M.T., 1992. Structural geology and geochronology of subduction complexes along the margin of Gondwanaland: New data from the Antarctic Peninsula and southernmost Andes, *Geol. Soc. Am. Bull.,* **104,** 1497–1514.

Hamilton, E.L., 1976. Shear-wave velocity versus depth in marine sediments: a review, *Geophysics,* **41,** 985–996.

Hamilton, E.L., 1978. Sound velocity gradients in marine sediments, *J. acoust. Soc. Am.,* **65,** 909–922.

Haq, B.U., 1998. Gas hydrates: Greenhouse nightmare? Energy panacea or pipe dream? *GSA Today,* **11,** 1–6.

Helgerud, M.B., Dvorkin, J., Nur, A., Sakai, A. & Collett, T., 1999. Elastic-wave velocity in marine sediments with gas hydrates: Effective medium modeling, *Geophys. Res. Lett.,* **26,** 2021–2024.

Holbrook, W.S., Hoskins, H., Wood, W.T., Stephen, R.A., Lizarralde, D. & Leg, 164 Science Party, 1996. Methane Hydrate and Free Gas on the Blake Ridge from Vertical Seismic Profiling, *Science,* **273,** 1840.

Hyndman, R.D. & Spence, G.D., 1992. A seismic study of methane hydrate marine bottom simulating reflector, *J. geoph. Res.,* **97,** 6683–6698.

Kim, Y., Kim, H.-S., Larter, R.D., Camerlenghi, A., Gambôa, L.A.P. & Rudowski, S., 1995. Tectonic deformation in the upper crust and sediments at the South Shetland trench, *AGU Antarctic Research Series,* **68,** 157–166.

Klepeis, K.A. & Lawver, L.A., 1996. Tectonics of the Antarctic–Scotia plate boundary near Elephant and Clarence Islands, West Antarctica, *J. geophys. Res.,* **101,** 20 211–20 231.

Kuster, G.T. & Toksöz, M.N., 1974. Velocity and attenuation of seismic waves in two-phase media: Part I, Theoretical formulations, *Geophysics,* **39,** 587–606.

Kvenvolden, K.A., 1998. A primer on the geological occurrence of gas hydrates, in *Gas Hydrates: Relevance to World Margin Stability and Climate Change, Geol. Soc., London, Spec. Pub., 137,* pp. 9–30, eds. Henriet, J.-P. & Mienert, J., Geological Society, London.

Larter, R.D. & Barker, P.F., 1991. Effects of ridge crest–trench interaction on Antarctic-Phoenix spreading: forces on a young subducting plate, *J. geophys. Res.,* **96,** 19 583–19 607.

Larter, R.D., Rebesco, M., Vanneste, L.E., Gambôa, P.A.P. & Barker, P.F., 1997. Cenozoic tectonic, sedimentary and glacial history of the continental shelf west of Graham Land, Antarctic Peninsula, *AGU Antarctic Research Series,* **71,** 1–27.

Leclaire, P., 1992. Propagation acoustique dans les milieux poreux soumis au gel-Modélisation et expérience, *PhD Thesis,* Université Paris 7, Paris.

Lee, M.Y., Hutchinson, D.R., Collet, T.S. & Dillon, W.P., 1996. Seismic velocities for hydrate-bearing sediments using weighted equation, *J. geophys. Res.,* **101,** 20 347–20 358.

Lodolo, E., Camerlenghi, A. & Brancolini, G., 1993. A bottom simulating reflector on the South Shetland Margin, Antarctic Peninsula, *Antarctic Sci.,* **5,** 207–210.

Lodolo, E., Tinivella, U., Pellis, G. & O.G.S.-Explora Party, 1998. Seismic investigation of the bottom simulating reflector on the South Shetland Margin, *Terra Antartica Rept.,* **2,** 71–74.

MacKay, M.E., Jarrard, R.D., Westbrook, G.K. & Hyndman, R.D., 1994. Origin of bottom simulating reflectors: geophysical evidence from the Cascadia accretionary prism, *Geology,* **22,** 459–462.

Maldonado, A., Larter, R.D. & Aldaya, F., 1994. Forearc tectonic evolution of the South Shetland Margin, Antarctic Peninsula, *Tectonics,* **13,** 1345–1370.

Markl, R.G., Bryan, G.M. & Ewing, J.I., 1970. Structure of the Blake-Bahama Outer Ridge, *J. geophys. Res.,* **75,** 4539–4555.

Miller, J.J., Lee, M.W. & von Huene, R., 1991. An analysis of a seismic reflection from the base of a gas hydrate zone, offshore Peru, *Am. Assoc Petrol Geol. Bull.,* **75,** 910–924.

Nolet, G., 1987. Seismic wave propagation and seismic tomography, in *Seismic tomography,* pp. 1–23, ed. Nolet, G., Reidel Dordrecht.

Paull, C.K., Matsumoto, R., Wallace, P.J. & Dillon, W.P. (eds), 2000, *.Proceedings of the ODP, Scientific Results,* 164, ODP Texas A & M University, College Station.

Pecher, I.A., Ranero, C.R., von Huene, R., Minshull, T.A. & Singh, S., 1998. The nature and distribution of bottom simulating reflectors at the Costa Rican convergent margin, *Geophys. J. Int.,* **133,** 219–229.

Rebesco, M., Camerlenghi, A. & Zanolla, C., 1998. Bathymetry and morphogenesis of the continental margin west of the Antarctic Peninsula, *Terra Antartica,* **5,** 715–725.

Rossi, G. & Vesnaver, A., 1997. 3D imaging by adaptive joint inversion of reflected and refracted arrivals, *Proc. SEG 67th Annual Meeting,* SEG, Dallas.

Ruppel, C. & Kinoshita, M., 2000. Fluid, methane, and energy flux in an active margin gas hydrate province, offshore Costa Rica, *Earth planet. Sci. Lett.,* **179,** 153–165.

Scholl, D.W. & Hart, P.E., 1997. Massive hydrate deposits in the Bering Sea basin: thoughts about their occurrence, origin, and resource potential, *First Annual Stanford Gas Hydrates Workshop (Abstracts), October, 21–22,* **1,** 33–35.

Schön, J.H., 1996. *Fundamentals and Principles of Petrophysics,* Pergamon Press, Oxford.

Shipley, T.H., Houston, M.H., Buffler, R.T., Shaub, F.J., McMillen, K.J., Ladd, J.W. & Worzel, J.L., 1979. Seismic evidence for widespread possible gas hydrate horizons on continental slopes and rises, *Am. Assoc. Petrol. Geol. Bull.,* **63,** 2204–2213.

Singh, S.C. & Minshull, T.A., 1994. Velocity structure of a gas hydrate reflector at Ocean Drilling Program Site 889 from global seismic waveform inversion, *J. geophys. Res.,* **99,** 24 221–24 233.

Singh, S.C., Minshull, T.A. & Spence, G.D., 1993. Velocity structure of a gas hydrate reflector, *Science,* **260,** 204–207.

Stewart, R.R., 1991. Exploration seismic tomography: fundamentals, *Course Note Series, 3,* Society of Exploration Geophysicists, Tulsa.

Suess, E., Bohrmann, G., von Huene, R., Linke, P., Wallmann, K., Lammers, S. & Sahling, H., 1998. Fluid venting in the Eastern Aleutian subduction zone, *J. geoph. Res.,* **103,** 2597–2614.

Suess, E., *et al.*, 1999. Gas hydrate destabilization: enhanced dewatering, benthic material turnover and large methane plumes at the Cascadia convergent margin, *Earth planet. Sci. Lett.,* **170,** 1–15.

Taner, M.T. & Köhler, F., 1969. Velocity spectra—digital computer derivation and application of velocity functions, *Geophysics,* **34,** 859–881.

Tinivella, U., 1999. A method for estimating gas hydrate and free gas concentrations in marine sediments, *Boll. Geof. Teor. Appl.,* **40,** 19–30.

Tinivella, U. & Accaino, F., 2000. Compressional velocity structure and Poisson's ratio in marine sediments with gas hydrate and free gas by inversion of reflected and refracted seismic data (South Shetland Islands, Antarctica), *Mar. Geol.,* **164,** 13–27.

Tinivella, U. & Lodolo, E. 2000 The Blake Ridge BSR, Tomographic Velocity Field and Theoretical Model to Estimate Methane Hydrate and Free Gas Quantities, *Proceedings of the ODP, Scientific Results,* 164, 273–281, eds Paull, C.K., Matsumoto, R., Wallace, P.J. and Dillon, W.P., ODP Texas A & M University, College Station.

Tinivella, U., Lodolo, E., Camerlenghi, A. & Böhm, G., 1998. Seismic tomography study of a bottom simulating reflector off the South Shetland Islands (Antarctica), in *Gas Hydrates: Relevance to World Margin Stability and Climate Change. Geological Society, London, Special Publication, 137,* pp. 141–151, eds Henriet, J.-P., & Mienert, J., Geological Society, London.

Tréhu, A., Torres, M.E., Moore, G.F. & Suess, E., 1999. Temporal and spatial evolution of a gas hydrate-bearing accretionary ridge on the Oregon continental margin, *Geology,* **27,** 939–942.

Van der Sluis, A. & Van der Vorst, H.A., 1987. Numerical solutions of large, sparse linear systems arising from tomographic problems, in *Seismic tomography,* pp. 49–84, ed. Nolet, G., Reidel Dordrecht.

Vesnaver, A., 1994. Towards the uniqueness of tomographic inversion solutions, *J. Seism. Explor.,* **3,** 323–334.

Vesnaver, A., 1996a. Irregular grids in seismic tomography and minimum time ray-tracing, *Geophys. J. Int.,* **125,** 641–165.

Vesnaver, A., 1996b. Ray-tracing based on Fermat's principle in irregular grids, *Geophys. Prospect.,* **44,** 741–760.

de Wit, M.J., 1977. The evolution of the Scotia Arc as a key to the reconstruction of the southwestern Gondwanaland, *Tectonophysics,* **37,** 53–81.

Wood, W.T., Stoffa, P.L. & Shipley, T.H., 1994. Quantitative detection of methane hydrayte through high-resolution seismic velocity analysis, *J. Geophys. Res.,* **99,** 9681–9695.

Worthington, M.H., 1984. An introduction to geophysical tomography, *First Break,* **2,** 20–26.

Yuan, T., Spence, G.D., Hyndman, R.D., Minshull, T.A. & Singh, S.C., 1999. Seismic velocity study of a gas hydrate bottom-simulating reflector on the northern Cascadia continental margin: Amplitude modeling and full waveform inversion, *J. Geophys. Res.,* **104,** 1179–1191.